Structural and Multidisciplinary Optimization (2024) 67:103
https://doi.org/10.1007/s00158-024-03824-9

RESEARCH

Mesh-based topology, shape and sizing optimization of ribbed plates

Oded Amir[1] · **Ahmad Majdouba**[2]

Received: 16 December 2023 / Revised: 24 April 2024 / Accepted: 21 May 2024 / Published online: 13 June 2024

Abstract
In this paper, we present a new parameterization and optimization procedure for minimizing the weight of ribbed plates. The primary goal is to reduce embodied CO_2 in concrete floors as part of the effort to diminish the carbon footprint of the construction industry. A coupled plate-beam finite element model and its computational mesh enable simultaneous topology, shape and sizing optimization of ribbed plate systems. Using analytical sensitivity analysis and gradient-based optimization, we achieve significant weight reductions in the range of 24–57%, in comparison to reference designs with regular ribbing patterns. The results strengthen the argument in favor of ribbed plates as a structural system that can serve the environmental goals of the construction industry. While our focus is on ribbed concrete plates in buildings, the proposed mesh-based design parameterization is applicable in the general case of optimizing stiffened shells—with potential contributions also to automotive and aerospace applications. All computer codes used in this study are freely available through a public repository, https://zenodo.org/records/11489996.

Keywords Topology optimization · Shape optimization · Ribbed plates · Concrete floors · Embodied CO_2

1 Introduction

Concrete is the most extensively used material in the construction industry worldwide. Reinforced and prestressed concrete structures are often the preferred choice due to various advantages, e.g., in terms of economy, durability and fire resistance. The popularity of concrete comes with a high environmental price tag: cement production is a major contributor to global CO_2 emissions, accounting for 7–8% and increasing steadily (Andrew 2019). The environmental impact of cement can be reduced by optimizing concrete structures, aiming to minimize embodied CO_2 (for example, Paya-Zaforteza et al. 2009; Yepes et al. 2012; Miller et al. 2015; Eleftheriadis et al. 2018; Jayasinghe et al. 2021; Pressmair et al. 2023). While minimizing concrete weight is not directly equivalent to minimizing embodied CO_2, it is clear that employing advanced shape and topology optimization techniques can lead to significant reduction in the use of raw materials. In the current work, we propose a formulation for comprehensive optimization of a specific type of concrete plate that can be used for reducing weight and embodied CO_2 of building floors: *ribbed plates* that comprise of a thin concrete plate, supported by a network of beams.

The term *ribbed plates* is used herein, but often there are other names that refer to the same structural system. In its simplest form, a ribbed plate consists of a series of parallel, unidirectional beams, creating T-sections with the top plate and acting in unidirectional bending. The most commonly applied ribbed plate system is the generalization to two-way bending, also known as a *waffle slab*. This system consists of a network of beams that are organized in a Cartesian pattern, typically aligning with the edges of the plate in case the floor layout is regular. A famous system of ribbed plates was developed by Pier Luigi Nervi, who positioned the beams according to the directions of principal bending moments, leading to irregular patterns that are both efficient and aesthetically appealing (Halpern et al. 2013). In several cases, the network of supporting beams is named a *grillage*—a term that literally refers to a series of co-planar beams that transfer transverse loads by out-of-plane bending.

Responsible Editor: Emilio Silva.

✉ Oded Amir
odedamir@technion.ac.il

[1] Faculty of Civil and Environmental Engineering, Technion – Israel Institute of Technology, Technion City, Haifa 3200003, Israel

[2] School of Architecture, Civil and Environmental Engineering, École polytechnique fédérale de Lausanne, GC A2 402 Station 18, 1015 Lausanne, Switzerland

Over the years, the optimization of ribbed plates has received attention from researchers in the field of structural optimization. The most frequently used representation is that of a grillage that undergoes layout optimization, extending the classical truss layout optimization. Analytical solutions to grillage optimization have been studied by Rozvany since 1972 (Rozvany 1972) and a thorough review can be found in Rozvany et al. (1995). Numerical approaches to grillage optimization are typically based on a ground structure parametrization, following its widespread application in truss layout optimization. This was first introduced by Sigmund et al. (1993) and has been further developed by Bolbotowski et al. (2018).

Recently, a detailed engineering design of reinforced concrete ribbed plates has been studied (Whiteley et al. 2023). In their work, the authors generated optimal grillage layouts by solving a plastic design formulation. The resulting optimization problems can be solved to global optimality by efficient linear programming techniques—an advantage in comparison to approach proposed herein, that leads to non-convex problems and can only find a local optimum. Subsequently, they designed reinforced concrete ribs and plates according to code requirements for ultimate limit states. In their interpretation, the ribs had uniform width and variable depth, leading to efficient utilization of material in bending. The weight of concrete was reduced by up to 30% compared to waffle slabs, showing the tremendous potential of employing advanced optimization for this class of structural systems. Another step towards practical application was presented by Huber et al. (2023), who designed the ribbing pattern according to the principal bending moments, following Nervi's approach. Subsequently, they performed sizing optimizations and adjustments of thicknesses near columns to avoid shear failures. Eventually, prototypes were fabricated with reinforced concrete using 3D-printed formwork to deal with the complex geometry. Weight savings of up to 40% compared to a solid slab have been reported.

Another approach to achieve optimum ribbed plates is by employing continuum topology optimization (Ma et al. 2023). The authors present two formulations. One is based on 3D continuum, where it is necessary to map the densities such that constructable ribs emerge without internal voids. The other is based on a shell model, where it is necessary to parameterize the thickness such that the domain is divided into regions of a thin plate and regions with additional ribs. The results benefit from the added design freedom compared to layout optimization, while constructability may be an issue because of the complex geometries that are characteristic of continuum topology optimization.

In a recent study (Majdouba 2022), a comprehensive computational exploration of optimized ribbed plates has been conducted. Two distinct parameterizations have been studied: (1) 3D continuum topology optimization with casting constraints, resembling the work of Ma et al. (2023; 2) Mesh-based topology, shape and sizing optimization of ribbed plates, relying on a plate-beam finite element model. Weight savings in the order of 20% compared to waffle slabs have been demonstrated, alongside two important findings: (1) The mesh-based optimization of plate-beam models achieved weight reductions that are close to those of continuum topology optimization, which in principle offers more design freedom for a much higher computational cost; (2) Optimized plate-beam models are more efficient than Nervi's patterns, leading to a weight reduction of roughly 10% more than Nervi's plates.

Building upon the preliminary results of Majdouba (2022), this paper presents the mesh-based optimization of plate-beam models. The key difference compared to grillage optimization is that the upper plate is modeled and coupled to the network of beams that are attached to it. This allows for consistent load transfer from the top surface to the beams when beams are eliminated and arbitrary spacing between beams is created. Another advantage is that the T-section behavior is automatically accounted for in the optimization. While in principle the mesh serves as a ground structure, we optimize also the nodal positions to relax the bias of the predefined ground structure and to get closer to a free-form optimization of the ribbed plate.

The remainder of the paper is organized as follows: The plate-beam finite element model is presented in Sect. 2. The optimization problem formulation and sensitivity analysis are presented in Sects. 3 and 4. Several numerical examples are shown in Sect. 5, emphasizing the comparison to traditional waffle slabs and the achieved relative weight savings. Finally, a concluding discussion is provided in Sect. 6.

2 The plate-beam model

2.1 Design parameterization

A key aspect of the current study is the design parameterization. The geometric parameters of the plate and beams that affect their stiffness are treated with topology and sizing variables. These include the plate thickness t and the beam depth h which are both uniform throughout the plate to promote constructability; and the beam widths b_i that are specific for each beam segment, are uniform along the length of the segment, and can be reduced to zero—enabling topology optimization of the layout. The layout of the beams is affected also by the coordinates of their nodes, that serve as shape variables. Conveniently, these nodes are the vertices of the triangulation of the upper plate. The main advantage of this parameterization is that when beams move or disappear (due to zero width), the bending of the plate is still modeled consistently. A

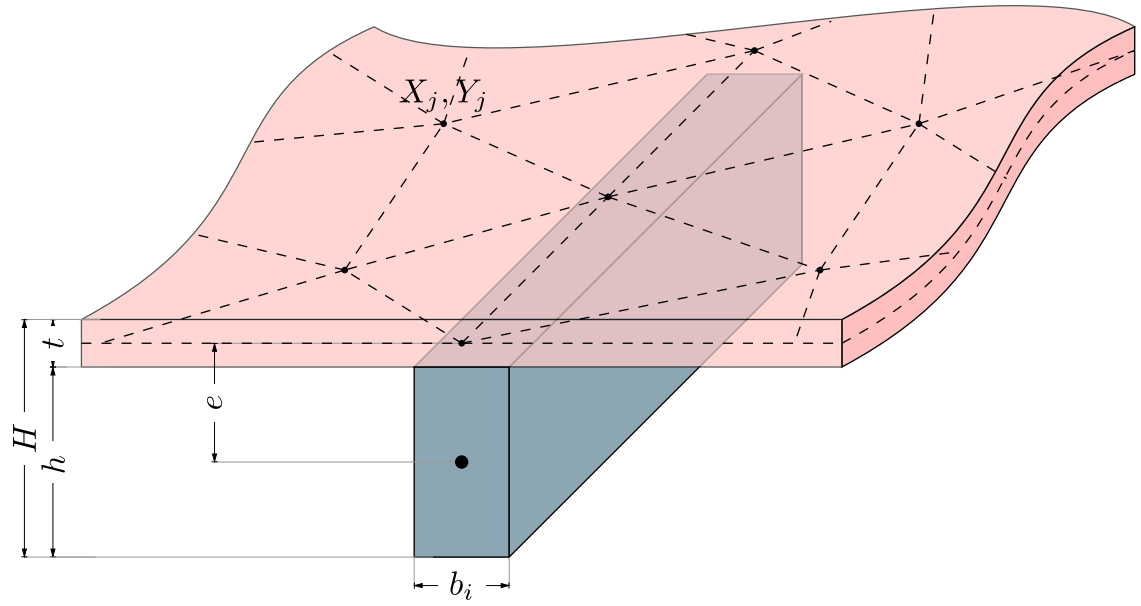

Fig. 1 Design parameterization of a ribbed plate system. The sketch shows a cut-out of the plate with a beam spanning two edges of the plate's triangulation. The stiffness is determined by the sizes t and h that together are constrained by the overall depth H; and by the width b_i that can vanish to zero. The shape of the layout is determined by optimizing the nodal coordinates $\{X_j, Y_j\}$

sketch of a small part of a plate with an attached beam is shown on Fig. 1. A key parameter that affects the coupling between the beam and the plate is the eccentricity $e = \frac{h}{2} + \frac{t}{2}$ which is design-dependent. Potentially, a beam segment can exist in every edge of the triangulation, meaning that the mesh plays the role of a 'ground structure' like in classical layout optimization (Dorn et al. 1964; Rozvany et al. 1995; Gilbert and Tyas 2003).

2.2 Finite element model

Simulation of the structural response is achieved by finite element analysis (FEA) of the plate and beams. This requires a model that captures the bending of the plate, the bending and torsion of the beams, and the T-section effect that arises from the in-plane stiffness of the plate. A schematic representation of the three types of finite elements that are combined in the current formulation is given in Fig. 2.

As there is no direct coupling between the membrane and bending behaviors of the plate itself, a triangular element can be created by superimposing a Constant Strain Triangle (CST) element, which models membrane behavior, and a Discrete Kirchhoff Theory (DKT) element, which models bending behavior. Upon assembly of these two components, a simple flat shell element is created with five degrees of freedom (DOF) per node j,

$$\{\mathbf{U}_j\}^T = \{u \quad v \quad w \quad \theta_x \quad \theta_y\}.$$

The CST element contributes to the membrane DOF

$$\{\mathbf{U}_j^{\mathrm{CST}}\}^T = \{u \quad v\} \tag{1}$$

which represent in-plane displacements. The DKT element contributes to the plate DOF

$$\{\mathbf{U}_j^{\mathrm{DKT}}\}^T = \{w \quad \theta_x \quad \theta_y\} \tag{2}$$

which represent the out-of-plane displacement and rotations. The stiffness matrix for a triangular CST element with DOF as in Eq. (1) is formulated following common FEA textbooks (e.g., Zienkiewicz and Taylor 2000; Bathe 1996; Cook et al. 2001). In formulating the stiffness matrix for the triangular DKT element with DOF as in Eq. (2), we follow the derivation of Batoz et al. (1980) and related work (Batoz 1982; Jeyachandrabose et al. 1985). Finally, at each node we add θ_z which is a drilling DOF that represents in-plane rotation. In the following, the plate's 18-by-18 element stiffness matrix is denoted $\mathbf{k}_{\mathrm{eP}}$. A detailed derivation of $\mathbf{k}_{\mathrm{eP}}$ in global coordinates is omitted herein for brevity, but the implementation in MATLAB (Mathworks 2023) is freely available for the readers. The stiffness coefficients on the diagonal entries corresponding to θ_z are given a value which is a small fraction of the diagonal entries corresponding to w. Therefore, the structure's stiffness w.r.t. drilling rotations is governed by the beams only.

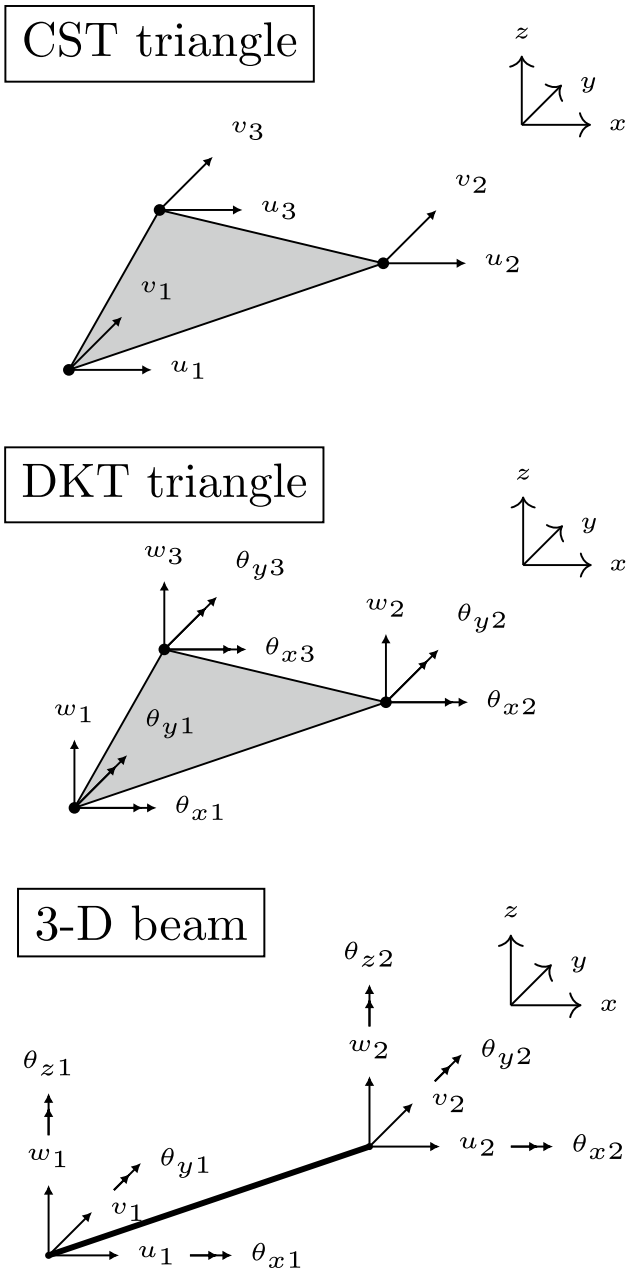

Fig. 2 CST, DKT and 3-D beam elements that are used in this work. The DOF are shown in global coordinates and local element-level numbering

The beam element is a standard two-node, three-dimensional Euler-Bernoulli beam element with a rectangular cross section (e.g., Weaver and Gere 2012). We take the torsional constant as $J_i = \beta h b_i^3$ for a certain beam segment i, assuming that $h \geq b_i$ and then $\beta = \frac{1}{3} - 0.21\frac{b_i}{h}\left(1 - \frac{b_i^4}{12h^4}\right)$. This condition is suitable in the current context because beams can only vanish by reducing their width b_i while the depth h is common for all beams and is larger than the maximal allowable b_i. Denoting the 12-by-12 beam stiffness matrix in its *local* coordinate system as $\mathbf{k}_{\mathrm{eB}}^{l}$, we first consider its eccentricity e w.r.t. the plate's mid plane,

$$\hat{\mathbf{k}}_{\mathrm{eB}}^{l} = \mathbf{T}^T \mathbf{k}_{\mathrm{eB}}^{l} \mathbf{T} \tag{3}$$

where $\mathbf{T}$ is a 12-by-12 matrix with entries $\mathbf{T}_{1,5} = -\mathbf{T}_{2,4} = \mathbf{T}_{7,11} = -\mathbf{T}_{8,10} = e$ and zeros otherwise. These entries reflect the coupling between displacements of the beam in parallel to the plate's plane and rotations of the plate's plane. Finally, the beam stiffness matrix in global coordinates is computed by applying the operator $\mathbf{R}$ that accounts for the relative rotation between the local and global coordinate systems,

$$\mathbf{k}_{\mathrm{eB}} = \mathbf{R}^T \hat{\mathbf{k}}_{\mathrm{eB}}^{l} \mathbf{R}. \tag{4}$$

The structure's stiffness matrix $\mathbf{K}$ is then a sum of all plate and beam element-level contributions, assembled according to global DOF numbering,

$$\mathbf{K} = \sum_{i=1}^{N_{\mathrm{P}}} \mathbf{k}_{\mathrm{eP},i} + \sum_{i=1}^{N_{\mathrm{B}}} \mathbf{k}_{\mathrm{eB},i} \tag{5}$$

where N_{P} is the number of plate elements; $\mathbf{k}_{\mathrm{eP},i}$ is the stiffness matrix of the i-th plate element; N_{B} is the number of beam elements; and $\mathbf{k}_{\mathrm{eB},i}$ is the stiffness matrix of the i-th beam element. We note that the displacement fields of the plate and beam elements are compatible not only at the nodes but also along the edges of the triangular elements, i.e., along the length of each beam segment. This is because the same interpolations are used in both types of elements: cubic for out-of-plane displacements and linear for in-plane displacements.

2.3 Verification

In principle, the combination of three types of finite elements does not impose any significant technical difficulty. Nevertheless, there is some room for errors in the derivation and implementation, of the DKT element in particular. Hence we present a verification of the implementation in which we solve a simple problem of a rectangular plate stiffened with two beams in a cross-like pattern, see Fig. 3. This example is taken from Chang (1973), specifically Table 4-15 in the reference where results using FEA are compared to results obtained with series expansions. The size of the rectangular plate is 0.762 m × 1.524 m, its thickness is 6.35 mm and it is simply supported in all four edges. Two beams are used to stiffen the plate, dividing it into four identical panels. The beams have cross-section sizes of 12.7 mm×127 mm in the x-direction and 12.7 mm×76.2 mm in the y-direction.

We use MATLAB's built-in PDE solver to mesh the domain with four levels of resolution, having maximum

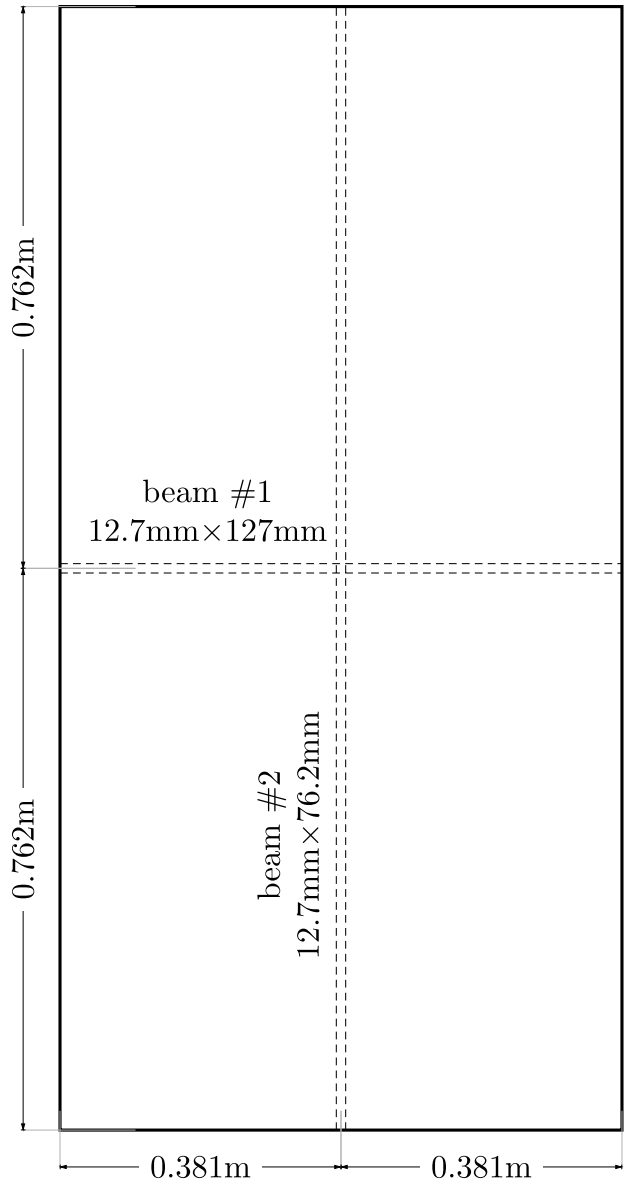

Fig. 3 An example of a rectangular plate stiffened by two beams (after Chang (1973)). All edges of the plate are simply supported

side lengths of 0.2, 0.1, 0.05 and 0.025. The numerical results of the vertical displacements at the center of the plate (the intersection of the beams) and at the center of each of the four panels are detailed in Table 1. It can be seen that our results are very close to the reference, in particular with the coarser meshes. A colored plot of the vertical displacements, computed using a mesh with maximum side length of 0.05, is presented in Fig. 4. The figure clearly shows the stiffening effect of the beams that restrain the deflections in the central axes of the plate.

Table 1 Verification of the implementation on the example of a stiffened rectangular plate

Mesh size	0.2	0.1	0.05	0.025	REF
w at center of plate	−0.2258	−0.2332	−0.2351	−0.2366	−0.2285
w at center of panel	−1.5683	−1.6348	−1.6457	−1.6702	−1.6300

The displacements are given in [m×10^{-3}]

3 Optimization problem formulation

The aim of optimization is to minimize the weight of the structure, while ensuring its structural integrity. In preliminary design of concrete structures, the geometry is determined according to service limit states which are usually defined in terms of allowable deformations. In the case of a plate or slab, a limit should be imposed on the

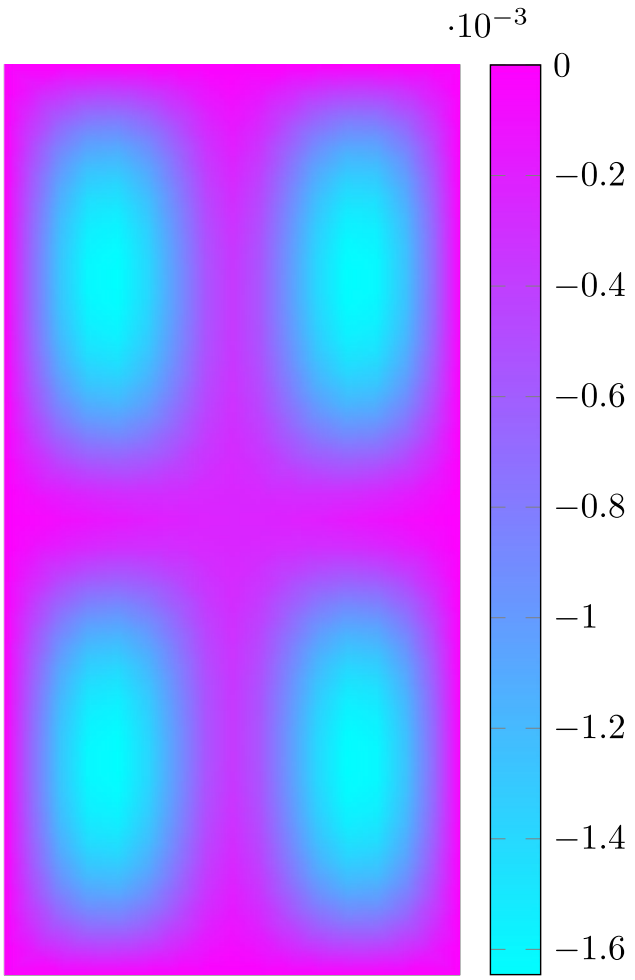

Fig. 4 Vertical displacements of the rectangular stiffened plate, computed using a mesh with maximum side length of 0.05. Numerical results are detailed in Table 1

maximal vertical displacement. This leads to the following problem formulation,

$$\begin{aligned} \underset{\mathbf{x}}{\text{minimize}} \quad & f_0(\mathbf{x}) = V_\mathrm{P} + V_\mathrm{B} \\ \text{subject to:} \quad & f_1(\mathbf{x}) = \frac{\hat{\delta}}{\delta^\star} - 1 \le 0 \\ & f_2(\mathbf{x}) = \frac{t+h}{\bar{H}} - 1 \le 0 \\ & \underline{\mathbf{x}} \le \mathbf{x} \le \bar{\mathbf{x}} \\ \text{subject to:} \quad & \mathbf{K}(\mathbf{x})\mathbf{u} = \mathbf{f}_{EXT} + \mathbf{f}_{SW} \end{aligned} \tag{6}$$

where $\mathbf{x}$ is a vector of *mathematical* design variables that are linked to *physical* design variables according to the specific context as detailed in the following.

3.1 Physical design variables

The first N_B design variables govern the widths b_i of each beam segment,

$$b_i(\mathbf{x}) = \underline{b} + (\bar{b} - \underline{b}) x_i^{p_b} \qquad i = 1, ..., N_\mathrm{B}$$

where $\underline{b}$ and $\bar{b}$ are lower and upper limits for the width and $0 \le x_i \le 1$. The limit $\underline{b}$ is chosen as a small number for numerical stability and $\bar{b}$ can be chosen based on design intentions. The exponent p_b is an optional SIMP-like penalty parameter. For $p_b = 1$, *sizing* of the beams is obtained, while for $p_b > 1$ intermediate widths are penalized and *topology* of the beam layout is gradually achieved, depending on the value of p_b and on the other geometric parameters.

The next two variables in the vector $\mathbf{x}$ govern the depth of the beams and the thickness of the plate, which are both uniform throughout the design domain to resemble the construction method of waffle slabs. These parameters are related to their design variables by linear interpolation,

$$h(\mathbf{x}) = \underline{h} + (\bar{h} - \underline{h}) x_{N_\mathrm{B}+1} \tag{7}$$

$$t(\mathbf{x}) = \underline{t} + (\bar{t} - \underline{t}) x_{N_\mathrm{B}+2} \tag{8}$$

where $\underline{h}$ is chosen as a small number for numerical stability, $\underline{t}$ is chosen based on engineering judgement, and

$$\begin{aligned} 0 \le & x_{N_\mathrm{B}+1} \le 1 \\ 0 \le & x_{N_\mathrm{B}+2} \le 1 \end{aligned}$$

Notice that there are no explicit values for $\bar{h}$ and $\bar{t}$. An upper limit $\bar{H}$ is imposed on the total depth H, so the upper limits are simply $\bar{h} = \bar{H} - \underline{t}$ and $\bar{t} = \bar{H} - \underline{h}$.

The last set of variables in the vector $\mathbf{x}$ governs the nodal coordinates, organized as follows

$$\begin{aligned} &\left\{ \hat{X}_1, \hat{Y}_1, ..., \hat{X}_j, \hat{Y}_j, ..., \hat{X}_{N_N}, \hat{Y}_{N_N} \right\} = \\ &\left\{ x_{N_\mathrm{B}+2+1}, x_{N_\mathrm{B}+2+2}, ..., x_{N_\mathrm{B}+2+2j-1}, \right. \\ &\left. x_{N_\mathrm{B}+2+2j}, ..., x_{N_\mathrm{B}+2+2N_N-1}, x_{N_\mathrm{B}+2+2N_N} \right\} \end{aligned} \tag{9}$$

where $j = 1, ..., N_N$ and N_N is the number of nodes. The coordinates $\hat{X}_j, \hat{Y}_j$ represent the raw design update that stems from the design vector $\mathbf{x}$ and the corresponding limits $\underline{\mathbf{x}}$ and $\bar{\mathbf{x}}$ are set according to the geometry of the domain. However, the actual nodal coordinates are determined after applying a few smoothing iterations, see Sect. 3.5. Equation (9) is written as if all nodes can move in both directions in the $x - y$ plane. Nevertheless, some movements are restricted according to the specific design domain. These coordinates are removed and re-introduced before and after design updates.

3.2 Volume objective function

The objective function is the volume of the structure, built up from the volume of the plate and the volume of the beams,

$$f_0(\mathbf{x}) = V_\mathrm{P} + V_\mathrm{B} = A_\mathrm{P} t(\mathbf{x}) + h(\mathbf{x}) \sum_{i=1}^{N_\mathrm{B}} b_i(\mathbf{x}) l_i(\mathbf{x}) \tag{10}$$

where A_P is the area of the plate which is constant; $t(\mathbf{x})$, $h(\mathbf{x})$ and $b_i(\mathbf{x})$ are the geometric parameters as detailed in Sect. 3.1; and $l_i(\mathbf{x})$ is the length of the i-th beam segment that depends on its nodal coordinates.

3.3 Constraints

The problem formulation (6) includes two general constraints. The constraint $f_1(\mathbf{x})$ limits the maximum deflection, where

$$\hat{\delta} = \|\boldsymbol{\delta}\|_\infty \tag{11}$$

and $\boldsymbol{\delta}$ contains all the vertical (or out-of-plane) displacements and is a subset of the displacements vector $\mathbf{u}$. The vector $\mathbf{u}$ depends implicitly on the design variables $\mathbf{x}$ through the equilibrium equations. The limit $\delta^\star$ is based on engineering requirements and is typically set to 1/750 of the span between supports. The definition (11) is not differentiable, meaning some smooth approximation should be employed. We replace $\hat{\delta}$ with its smooth counterpart,

$$\widetilde{\delta} = \|\boldsymbol{\delta}\|_{p_\delta} \tag{12}$$

and use $p_\delta = 16$ throughout all numerical examples. However, in order to avoid rescaling of the threshold $\delta^\star$ to accommodate the over-estimation of the p-norm, the optimizer is given the value of the true constraint (11) and the derivatives

are taken by differentiation of $\widetilde{\delta}$. This strategy works well and no problems are encountered with satisfying the deflection constraint.

The second constraint $f_2(\mathbf{x})$ limits the overall depth of the ribbed plate system to a prescribed value $\bar{H}$, and depends explicitly on $\mathbf{x}$ through Eqs. (7) and (8). Clearly, for stiffness it is best to increase the depth, in particular of the beams. On the other hand, increasing the overall depth has negative architectural implications because it limits the usable height of the storey. Furthermore, increasing the overall storey height may increase the overall cost of the building. This trade-off will be addressed in some of the examples in Sect. 5. Notice that the parameter $\bar{H}$ indirectly limits the maximal depth of the beams and thickness of the plate, as discussed in Sect. 3.1.

3.4 Equilibrium equations

The ultimate component of (6) are the equilibrium equations, where the stiffness matrix $\mathbf{K}(\mathbf{x})$ is formulated based on Eqs. (3), (4) and (5). It depends explicitly on all types of design variables. The force vector $\mathbf{f}_{EXT}(\mathbf{x})$ represents the external load applied on the plate's surface, which is distributed uniformly in the current context. This vector is assembled from the individual contributions of each plate element according to the area of the triangular element that depends on its nodal coordinates. Therefore, while $\mathbf{f}_{EXT}(\mathbf{x})$ is always *physically* uniform, its distribution to nodal loads depends on $\mathbf{x}$ through the nodal coordinates and hence is design-dependent. The second part of the force vector, $\mathbf{f}_{SW}(\mathbf{x})$, is the load due to self-weight of the structure. It depends explicitly on all types of design variables: the weight of the plate depends on $t(\mathbf{x})$ and its nodal distribution depends on the coordinates; similarly, the weight of the beams depends on $h(\mathbf{x})$, $b_i(\mathbf{x})$ and $l_i(\mathbf{x})$.

3.5 Mesh smoothing

One part of the design parameterization are the nodal locations which are controlled by shape design variables. This means that the mesh changes its shape without updating the connectivity, and some acute distortions may occur. To reduce distortion we apply a simple form of Laplacian smoothing, that recursively places each node according to the average of the nodes that are connected to it (Field 1988),

$$X_j = \frac{1}{N_j}\sum\nolimits_{k\in\mathbf{X}_j} \hat{X}_k$$
$$Y_j = \frac{1}{N_j}\sum\nolimits_{k\in\mathbf{X}_j} \hat{Y}_k$$

where N_j is the number of vertices that are connected by an edge to the vertex j, $\mathbf{X}_j$ is the set of indices of vertices that are connected by an edge to the vertex j and the coordinates $\hat{X}_m$, $\hat{Y}_m$ are directly related to the design variables, see Eq. (9). This is a rather naive approach but it performs sufficiently well for the purpose of the current study. Because the mesh connectivity is unaltered during optimization, the coefficients for each nodal coordinate can be computed prior to the optimization and are collected in the matrix $\mathbf{L}$. As some nodal movements are restricted in either one or two directions, the application of $\mathbf{L}$ may differ between directions, hence

$$\begin{aligned}\mathbf{X} &= \mathbf{L}_X^{N_\mathrm{L}}\hat{\mathbf{X}}\\ \mathbf{Y} &= \mathbf{L}_Y^{N_\mathrm{L}}\hat{\mathbf{Y}}\end{aligned} \tag{13}$$

where $\mathbf{L}_X$ and $\mathbf{L}_Y$ are adaptations of $\mathbf{L}$ to the specific active and passive nodes in each direction, and N_L is the number of smoothing cycles.

4 Sensitivity analysis

To solve the optimization problem in Eq. (6), we employ sequential convex programming, specifically MMA (Svanberg 1987). As a first-order algorithm, MMA requires an evaluation of the objective and constraints, as well as their first-order derivatives. All derivatives are formulated analytically and the numerical implementation is verified by comparison to finite differences. However, a complete description of the derivations is lengthy and may not be useful to the readers. We resort to a brief presentation of the main components, that together with the available MATLAB codes can provide the readers with a complete understanding of the sensitivity analysis. We note that due to the complexity of some of the derivatives, manual derivation is challenging so analytical differentiation with MATLAB's symbolic engine was used. Symbolic expressions were then converted to numerical function calls for executing the optimization.

In the following, we provide general expressions of the derivatives w.r.t. all types of physical design variables according to their exposition in Sect. 3.1. The chain rule is subsequently applied to obtain the derivatives w.r.t. $\mathbf{x}$. For brevity, nodal coordinates after smoothing, i.e. $\{X_j, Y_j\}$, are represented here as a generic coordinate C_j.

4.1 Volume objective function

Observing Eq. (10), the volume objective has explicit derivatives w.r.t all types of design variables,

$$\frac{\partial f_0}{\partial b_i} = h l_i$$
$$\frac{\partial f_0}{\partial h} = \sum_{i=1}^{N_\mathrm{B}} b_i l_i$$
$$\frac{\partial f_0}{\partial t} = A_\mathrm{P}$$
$$\frac{\partial f_0}{\partial C_j} = h \sum_{i \in \Omega_j} b_i \frac{\partial l_i}{\partial C_j}$$

where Ω_j defines the set of edges in the mesh that is connected to the j-th node, so that the derivative of $\frac{\partial l_i}{\partial C_j}$ contributes to $\frac{\partial f_0}{\partial C_j}$.

4.2 Deflection constraint

As explained above, the derivative of $f_1(\mathbf{x})$ is computed according to the smooth approximation of the maximum deflection, Eq. (12). Applying an adjoint technique to eliminate the implicit dependence on the state $\mathbf{u}$, the derivative w.r.t. a generic physical design variable ξ is

$$\frac{\partial f_1}{\partial \xi} = \frac{1}{\delta^\star} \lambda^T \left(\frac{\partial \mathbf{K}}{\partial \xi}\mathbf{u} - \frac{\partial \mathbf{f}_{EXT}}{\partial \xi} - \frac{\partial \mathbf{f}_{SW}}{\partial \xi} \right) \tag{14}$$

with the adjoint vector computed from the equation

$$\mathbf{K}^T \lambda = -\left(\frac{\partial \widetilde{\delta}}{\partial \mathbf{u}} \right)^T \quad . \tag{15}$$

Since $\widetilde{\delta}$ is simply an aggregation of vertical displacements, the right-hand-side of Eq. (15) is a vector with entries $\left(\sum_{i=1}^{N_N} \mathbf{u}_{6i-3}^{p_\delta} \right)^{\frac{1}{p_\delta}-1} \mathbf{u}_{6i-3}^{p_\delta - 1}$ at the third DOF of each node i and zeros otherwise.

Once the adjoint vector is computed, the three separate terms in Eq. (14) can be evaluated. These depend on the specific context of ξ, whether it represents b_i, h, t or C_j. In the following, the index i refers to a certain element that can be either a plate or a beam. Furthermore, the notations eP and eB are used to designate element-level expressions such as stiffness or loads, for plates and beams respectively.

The case of ξ representing b_i, the width of beam element i:

$$\lambda^T \frac{\partial \mathbf{K}}{\partial \xi}\mathbf{u} = \lambda^T \frac{\partial \mathbf{K}}{\partial b_i}\mathbf{u} = \lambda_i^T \frac{\partial \mathbf{k}_{\mathrm{eB},i}}{\partial b_i}\mathbf{u}_i \quad ,$$
$$\lambda^T \frac{\partial \mathbf{f}_{EXT}}{\partial \xi} = \lambda^T \frac{\partial \mathbf{f}_{EXT}}{\partial b_i} = 0 \quad ,$$
$$\lambda^T \frac{\partial \mathbf{f}_{SW}}{\partial \xi} = \lambda^T \frac{\partial \mathbf{f}_{SW}}{\partial b_i} = \lambda_i^T \frac{\partial \mathbf{f}_{SW,i}}{\partial b_i} \quad .$$

The case of ξ representing h, the height of all beams:

$$\lambda^T \frac{\partial \mathbf{K}}{\partial \xi}\mathbf{u} = \lambda^T \frac{\partial \mathbf{K}}{\partial h}\mathbf{u} = \sum_{i=1}^{N_\mathrm{B}} \lambda_i^T \frac{\partial \mathbf{k}_{\mathrm{eB},i}}{\partial h}\mathbf{u}_i \quad ,$$
$$\lambda^T \frac{\partial \mathbf{f}_{EXT}}{\partial \xi} = \lambda^T \frac{\partial \mathbf{f}_{EXT}}{\partial h} = 0 \quad ,$$
$$\lambda^T \frac{\partial \mathbf{f}_{SW}}{\partial \xi} = \lambda^T \frac{\partial \mathbf{f}_{SW}}{\partial h} = \lambda^T \sum_{i=1}^{N_\mathrm{B}} \frac{\partial \mathbf{f}_{SW,i}}{\partial h} \quad .$$

The case of ξ representing t, the thickness of the plate:

$$\lambda^T \frac{\partial \mathbf{K}}{\partial \xi}\mathbf{u} = \lambda^T \frac{\partial \mathbf{K}}{\partial t}\mathbf{u} = \sum_{i=1}^{N_\mathrm{P}} \lambda_i^T \frac{\partial \mathbf{k}_{\mathrm{eP},i}}{\partial t}\mathbf{u}_i + \sum_{i=1}^{N_\mathrm{B}} \lambda_i^T \frac{\partial \mathbf{k}_{\mathrm{eB},i}}{\partial t}\mathbf{u}_i \quad ,$$
$$\lambda^T \frac{\partial \mathbf{f}_{EXT}}{\partial \xi} = \lambda^T \frac{\partial \mathbf{f}_{EXT}}{\partial t} = 0 \quad ,$$
$$\lambda^T \frac{\partial \mathbf{f}_{SW}}{\partial \xi} = \lambda^T \frac{\partial \mathbf{f}_{SW}}{\partial t} = \lambda^T \sum_{i=1}^{N_\mathrm{P}} \frac{\partial \mathbf{f}_{SW,i}^{\mathrm{eP}}}{\partial t} \quad ,$$

where we note that the stiffness of a beam element $\mathbf{k}_{\mathrm{eB},i}$ depends on t due to the eccentricity e.

The case of ξ representing C_j, a certain node coordinate:

$$\lambda^T \frac{\partial \mathbf{K}}{\partial \xi}\mathbf{u} = \lambda^T \frac{\partial \mathbf{K}}{\partial C_j}\mathbf{u} = \sum_{i \in \Omega_j} \lambda_i^T \frac{\partial \mathbf{k}_{\mathrm{eP},i}}{\partial C_j}\mathbf{u}_i + \sum_{i \in \Omega_j} \lambda_i^T \frac{\partial \mathbf{k}_{\mathrm{eB},i}}{\partial C_j}\mathbf{u}_i \quad ,$$
$$\lambda^T \frac{\partial \mathbf{f}_{EXT}}{\partial \xi} = \lambda^T \frac{\partial \mathbf{f}_{EXT}}{\partial C_j} = \sum_{i \in \Omega_j} \lambda_i^T \frac{\partial \mathbf{f}_{EXT_i}^{\mathrm{eP}}}{\partial C_j} \quad ,$$
$$\lambda^T \frac{\partial \mathbf{f}_{SW}}{\partial \xi} = \lambda^T \frac{\partial \mathbf{f}_{SW}}{\partial C_j} = \sum_{i \in \Omega_j} \lambda_i^T \frac{\partial \mathbf{f}_{SW,i}^{\mathrm{eP}}}{\partial C_j} + \sum_{i \in \Omega_j} \lambda_i^T \frac{\partial \mathbf{f}_{SW,i}^{\mathrm{eB}}}{\partial C_j} \quad .$$

In the derivations above, the element-level terms $\frac{\partial \mathbf{k}_{\mathrm{eB},i}}{\partial b_i}$, $\frac{\partial \mathbf{f}_{SW,i}}{\partial b_i}$, $\frac{\partial \mathbf{k}_{\mathrm{eB},i}}{\partial h}$, $\frac{\partial \mathbf{f}_{SW,i}}{\partial h}$, $\frac{\partial \mathbf{k}_{\mathrm{eP},i}}{\partial t}$, $\frac{\partial \mathbf{k}_{\mathrm{eB},i}}{\partial t}$, $\frac{\partial \mathbf{f}_{SW,i}^{\mathrm{eP}}}{\partial t}$, $\frac{\partial \mathbf{k}_{\mathrm{eP},i}}{\partial C_j}$, $\frac{\partial \mathbf{k}_{\mathrm{eB},i}}{\partial C_j}$, $\frac{\partial \mathbf{f}_{EXT_i}^{\mathrm{eP}}}{\partial C_j}$, $\frac{\partial \mathbf{f}_{SW,i}^{\mathrm{eP}}}{\partial C_j}$ and $\frac{\partial \mathbf{f}_{SW,i}^{\mathrm{eB}}}{\partial C_j}$ are not provided in detail but can be understood from the implementation. Finally, we note that all derivatives w.r.t. C_j need to pass through the chain rule to account for the smoothing operations of Eq. (13).

5 Design examples

Several design examples are presented in this section that demonstrate the outcomes of the proposed mesh-based topology, shape and sizing optimization of ribbed plates. We show four different cases in terms of the plate's design domain and boundary conditions. The first three cases have square domains, so we compare the optimized volume to a reference waffle slab. The fourth case is a trapezoidal layout so we assume a reference design with a triangular pattern of ribs. To determine a reference design, a total depth is first assumed based on thumb rules and

Table 2 Numerical parameters common to all examples

Description	Symbol	Value
Young's modulus	E	30e6 kN/m^2
Poisson's ratio	ν	0.2
Concrete specific weight	ρ	25 kN/m^3
External load	f	5 kN/m^2
Maximum optimization iterations	N_O	100
Stopping tolerance	ε	1e-3
External MMA move limit for topology/sizing	s_1	0.2
External MMA move limit for nodes	s_2	0.05
Minimal beam width	$\underline{b}$	1e-3
Optional SIMP penalty	p_b	from 1 to 3, every 25 iter
Minimal beam depth	$\underline{h}$	1e-3
Laplacian smoothing iterations	N_L	10

the plate thickness is chosen as roughly 20% of the total depth. Then, the beam layout is assumed to be parallel to the plate edges and the beam widths are assumed uniform. By trial and error, the beam width can be found for which the maximum deflection satisfies the design requirement of 1/750 of the span. The examples share a common set of numerical parameters that are detailed and explained in Table 2. Additional specific parameters and specific choices that are different from the default, are detailed in the text.

When optimizing the plate's structural parameters, there are two competing goals in mind: 1) Minimizing the volume, which directly affects the amount of material resources invested in the plate itself and indirectly in the vertical system of the building; 2) Minimizing the total depth, which indirectly affects costs and benefits of the complete building, e.g., architectural height of a floor, total height of the building, cost of external cladding, and magnitude of horizontal forces. We do not attempt to provide a complete trade-off study herein but the effect of the total available depth will be shown in the numerical results.

Solutions of the optimization problem (6) are sought by MMA (Svanberg 1987). In the numerical experiments, it was observed that MMA is more stable when splitting the design updates to two phases within each design cycle: first, the variables that govern b_i, h and t are updated, and subsequently the variables that govern nodal positions are updated. Given the non-convex nature of the optimization problem, we only expect to find local minima solutions. The results hereafter have been obtained after some numerical experimentation, aiming to find a common set of parameters that yield consistent results for all examples—in terms of weight savings and constraint feasibility. We did not conduct further experiments to determine whether better minima could be found.

5.1 Example 1: 10-by-10, simply supported

In this example, we optimize a 10 m-by-10 m plate with vertical supports in all edges—resembling a plate supported by stiff beams. Our reference design is based on the common waffle-like pattern with $H = 0.4$m and $t = 0.08$m. The beam width is $b_i = 0.1$m for all beams and the grid consists of 16-by-16 voids. The overall volume is 18.88 m^3 and the maximum vertical deflection is 0.0126 m. The plate's vertical deflections are displayed in Fig. 5, superimposed on a two-dimensional view of the beam layout.

Utilizing double symmetry, we optimize the bottom-left quadrant, a 5 m-by-5 m domain with a triangular mesh consisting of 145 nodes, 400 edges and 256 triangles. The boundary conditions for displacements and rotations, the restricted node movements for shape optimization and the initial mesh are sketched in Fig. 6. In the initial design prior to optimization, the plate thickness is $t = 0.1$m, the beam depth is $h = 0.2$m and all the beams are assigned $b_i = 0.1$m.

Table 3 and Fig. 7 show the results of three optimization runs, displayed on the full 10 m-by-10 m plate. In all three cases, the maximum beam width is $\bar{b} = 0.12$m. Runs #1 and #2 are with a total depth of $\bar{H} = 0.35$m whereas run #3 is with $\bar{H} = 0.40$m. Accordingly, $\underline{t} = 0.07$m in runs #1 and #2 and $\underline{t} = 0.08$m in run #3. Finally, run #1 applies sizing to the beam widths while runs #2 and #3 include a SIMP penalty to promote a uniform cross-section of all beams.

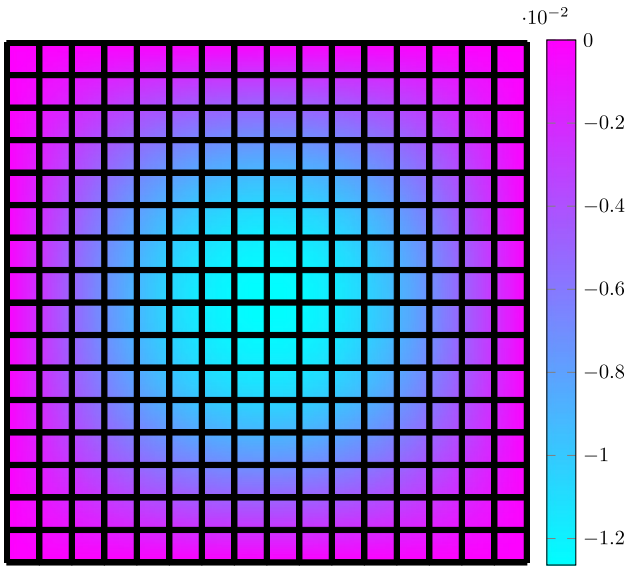

Fig. 5 Waffle-pattern reference design for a simply supported plate, Example 1. The volume is 18.88 m^3 and the maximum deflection is 0.0126 m

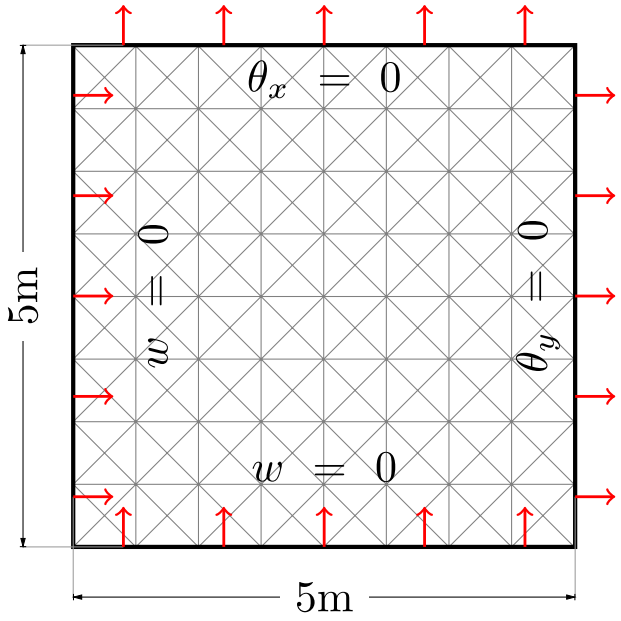

Fig. 6 Problem setup for the bottom left quarter of a simply supported plate, Example 1. The boundary conditions are stated along each edge. Red arrows represent restricted directions for node movements along the boundaries and gray lines represent the initial mesh

The results show that the simultaneous topology-shape-sizing optimization of the plate-beam system can lead to significant weight savings that exceed 30%, without increasing (and in some cases with decreasing) the total depth. Mesh movement together with elimination of beams create irregular spaces between beams, whose deflection is evaluated consistently with the plate-beam model. We see that in the sizing formulation (run #1) there were relatively large mesh movements and stiff diagonal regions were created by closing the gaps between beams via mesh distortion. The effect of artificial plate stiffness due to mesh distortion is discussed and quantified in Sect. 5.4. As expected, fewer beams are used when applying a SIMP penalty and when increasing the total depth—the latter tendency is explained by the relatively higher stiffness-to-weight ratio of deep beams, hence the optimizer chooses fewer beams that utilize the available depth.

5.2 Example 2: 10-by-10 on 4 columns, fixed conditions

In this example, we optimize a 10 m-by-10 m plate supported on 4 columns at the corners. The columns have fixed conditions—meaning they restrain vertical displacements and out of plane rotations. These conditions can model a single internal span of a floor where the adjacent spans restrain rotations above the columns and continuity of bending moments is possible. Our reference design is again a waffle-like structure, with $H = 0.53$m and $t = 0.08$m. The beam width is $b_i = 0.1$m for all beams and the grid consists of 16-by-16 voids. The overall volume is 23.30 m^3 and the maximum deflection is 0.013 m. The plate's deflections are displayed in Fig. 8, superimposed on a two-dimensional view of the beam layout.

Double symmetry is utilized again and the initial mesh is the same as in Example 1. The boundary conditions for displacements and rotations, the restricted node movements for shape optimization and the initial mesh are sketched in Fig. 9. In the initial design prior to optimization, the plate thickness is $t = 0.1$m, the beam depth is $h = 0.3$m and all the beams are assigned $b_i = 0.1$m. When solving this setup, relatively larger mesh movements have been observed compared to Example 1. To avoid severe mesh distortion, a more conservative move limit was chosen, $s_2 = 0.025$. To balance this conservative measure, the number of smoothing steps was reduced to $N_L = 5$. Based on extensive numerical experimentation, we can say that in general the computational procedure produces good results for various combinations of s_2 and N_L, but a complete parametric study towards optimal choices of the parameters is beyond the current scope.

Table 4 and Fig. 10 show the results of three optimization runs. In all three cases, the maximum beam width is $\bar{b} = 0.12$m. Runs #1 and #2 are with a total depth of $\bar{H} = 0.48$m whereas run #3 is with $\bar{H} = 0.53$m, and $\underline{t} = 0.08$m in all runs. Finally, run #1 applies sizing to the beam widths while runs #2 and #3 include a SIMP penalty to promote a uniform cross-section of all beams.

The results show again that the simultaneous optimization of the plate-beam system can lead to significant weight savings that herein exceed 40% in one case. Again, these savings are achieved with the same total depth as in the

Table 3 Numerical results of Example 1

run	p_b	$\bar{H}$[m]	$\underline{t}$	iters	t[m]	h[m]	δ [m]	V [m^3]
#1	1	0.35	0.07	100	0.07	0.28	0.0126	11.8211 (-37%)
#2	3	0.35	0.07	90	0.07	0.28	0.0126	13.3781 (-29%)
#3	3	0.40	0.08	88	0.08	0.32	0.0126	12.4635 (-34%)

All runs use their minimal allowable t and maximal allowable depth H. The deflection constraint is satisfied precisely. The rightmost column includes the savings in volume, compared to the reference design

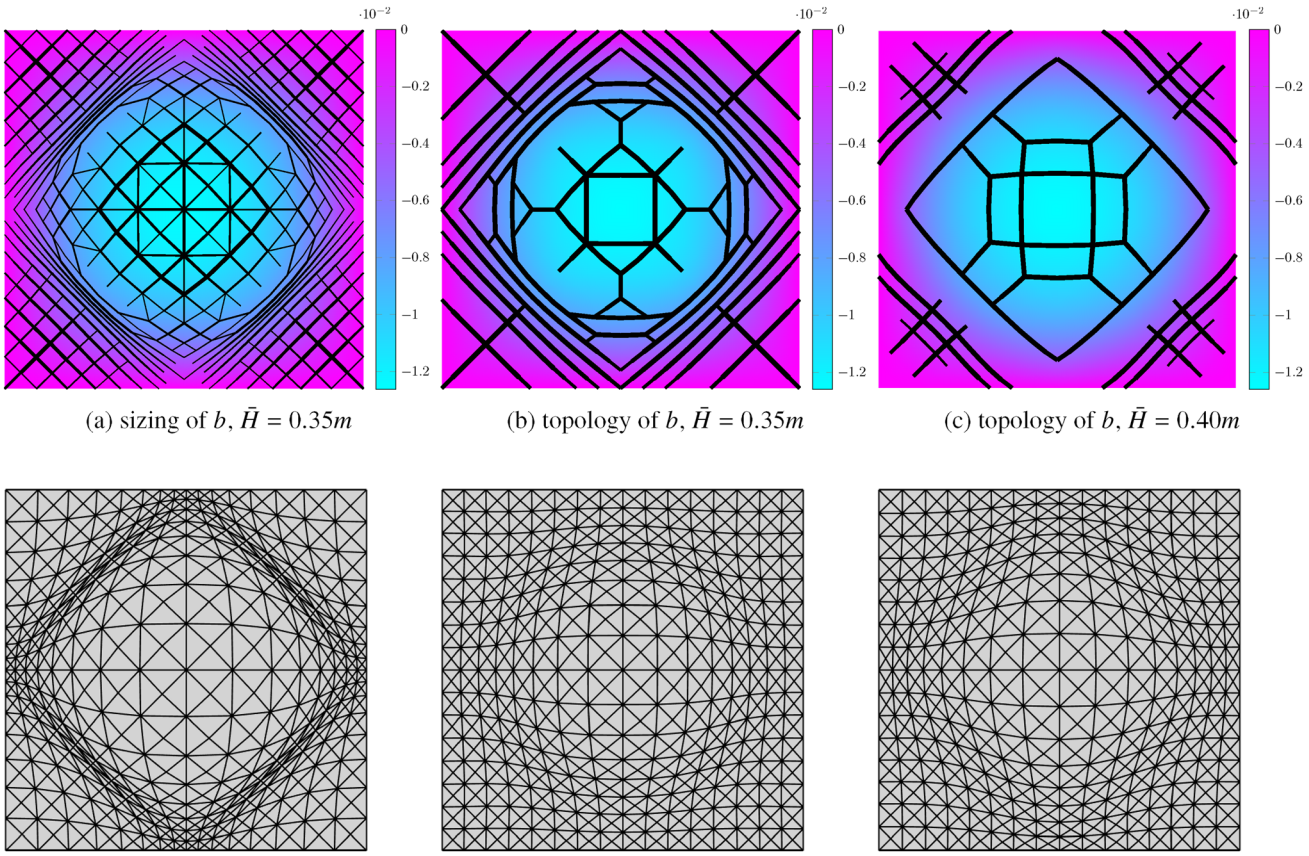

(a) sizing of b, $\bar{H} = 0.35m$ (b) topology of b, $\bar{H} = 0.35m$ (c) topology of b, $\bar{H} = 0.40m$

Fig. 7 Optimized layouts (black lines) and vertical displacements (colored map) of Example 1, a 10-by-10 simply supported plate. The second row shows the optimized meshes

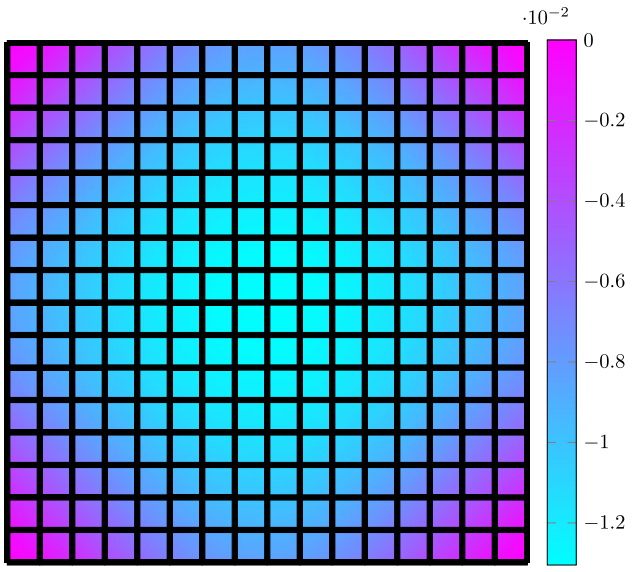

Fig. 8 Waffle-pattern reference design for a plate on four fixed columns, Example 2. The volume is 23.30 m^3 and the maximum deflection is 0.0130 m

reference design, or with a smaller depth. The mesh movement is somewhat more subtle than in Example 1, due to the more conservative move limit. Still, the mesh optimization allows to create variable spacing between beams and arbitrarily shaped voids that contribute to the weight savings.

5.3 Example 3: 10-by-10 on 4 columns, with cantilevers

In this example, we optimize a 10 m-by-10 m plate supported on 4 columns that are positioned internally, leaving a cantilevered strip of 1.875 m in all edges of the plate. The columns restrain only vertical displacements and bending resistance comes from the loads on the cantilevers. Our reference design consists again of 16-by-16 voids organized in an orthogonal pattern. The total depth is 0.27 m, of which the plate is 0.05 m, and the beam width is 0.1 m for all beams. The overall volume is 12.48 m^3 and the maximum deflection is 0.0108 m. The plate's deflections are shown in Fig. 11, superimposed on a two-dimensional view of the beam layout.

Double symmetry is utilized and the initial mesh is the same as in the previous examples. The boundary

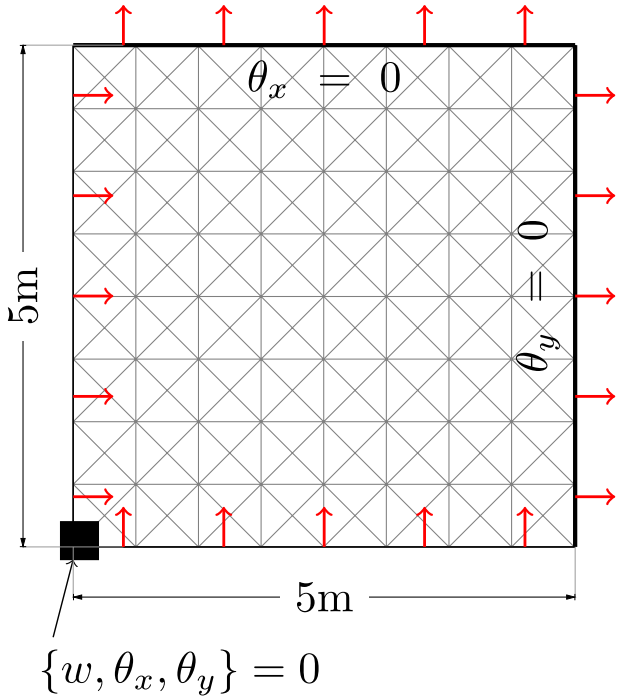

Fig. 9 Problem setup for the bottom left quarter of a plate on 4 columns, Example 2. The boundary conditions are stated along the symmetric edges and near the column. Red arrows represent restricted directions for node movements along the boundaries and gray lines represent the initial mesh

conditions for displacements and rotations, the restricted node movements for shape optimization and the initial mesh are sketched in Fig. 12. In the initial design prior to optimization, the plate thickness is $t = 0.07$m, the beam height is $h = 0.15$m and all the beams are assigned $b_i = 0.1$ m.

Table 5 and Fig. 13 show the results of three optimization runs. In all three cases, the maximum beam width is $\bar{b} = 0.12$m. Runs #1 and #2 are with a total depth of $\bar{H} = 0.25$m whereas run #3 is with $\bar{H} = 0.27$m, and $\underline{t} = 0.05$m in all runs. Finally, run #1 applies sizing to the beam widths while runs #2 and #3 include a SIMP penalty to promote a uniform cross-section of all beams.

The displacement maps in Fig. 13 reveal an interesting, non-trivial optimized design: while the uniform reference design exhibits upwards displacements of the cantilevered corners—which are nearly half of the downwards displacement in the center—the optimized designs reduce these displacements, and in some cases eliminate them. It is known that for such a cantilevered plate, maximum stiffness is achieved when the columns are positioned such that there is zero rotation above the columns (Mróz and Rozvany 1975; Fuchs and Brull 1979; Zelickman and Amir 2022). Given that the locations of the columns are fixed, the optimization aims at a similar goal by manipulating the stiffness of the internal span and the cantilevers. Another noticeable manipulation are the larger displacements along the plate's edges, compared to the reference design. The optimized designs show better utilization of the design space by bringing several regions close to the deflection constraint, while in the reference design the maximal deflection is obtained in the center and the displacements along the edges are much lower. This type of design intervention was not possible in the previous two examples, hence the displacements of the optimized designs were very similar to the reference responses. We notice that the node movements are not significant in this example, except perhaps for some curvatures near the columns in run #3.

5.4 Example 4: Trapezoidal domain on 4 columns, fixed conditions

One of the attractive features of the current design parameterization is that any domain shape can be treated, based on a triangular mesh of the surface. In this example, we optimize a trapezoidal plate which is supported at its vertices on 4 columns that have fixed conditions. The trapezoidal shape is created by trimming an equilateral triangle with side length of 12 m. Generating a traditional design for this domain is not as straightforward as for the rectangular domains. We choose a ribbing pattern based on a coarse triangulation of the domain, with beams placed every 1 m. The reference design has a total depth of 0.42 m, of which the plate is 0.07 m, and the beam width is 0.12 m for all beams. The overall volume is 12.62 m ^{3} and the maximum deflection is 0.015 m. This value meets the requirement w.r.t. the critical span between columns which is 12 m. The plate's deflections are displayed upon the design in Fig. 14. The relative inefficiency of a uniform triangular design can be inferred from the deflection map: there are three stiff edges where the deflections are close to zero, and the allowable deflection is observed only along the long edge.

Table 4 Numerical results of Example 2

run	p_b	$\bar{H}$[m]	$\underline{t}$	iters	t[m]	h[m]	δ [m]	V [m^3]
#1	1	0.48	0.08	100	0.08	0.40	0.0130	14.2519 (-39%)
#2	3	0.48	0.08	72	0.08	0.40	0.0130	15.8755 (-32%)
#3	3	0.53	0.08	87	0.08	0.45	0.0130	13.5704 (-42%)

All runs use their minimal allowable t and maximal allowable depth H. The deflection constraint is satisfied precisely. The rightmost column includes the savings in volume, compared to the reference design

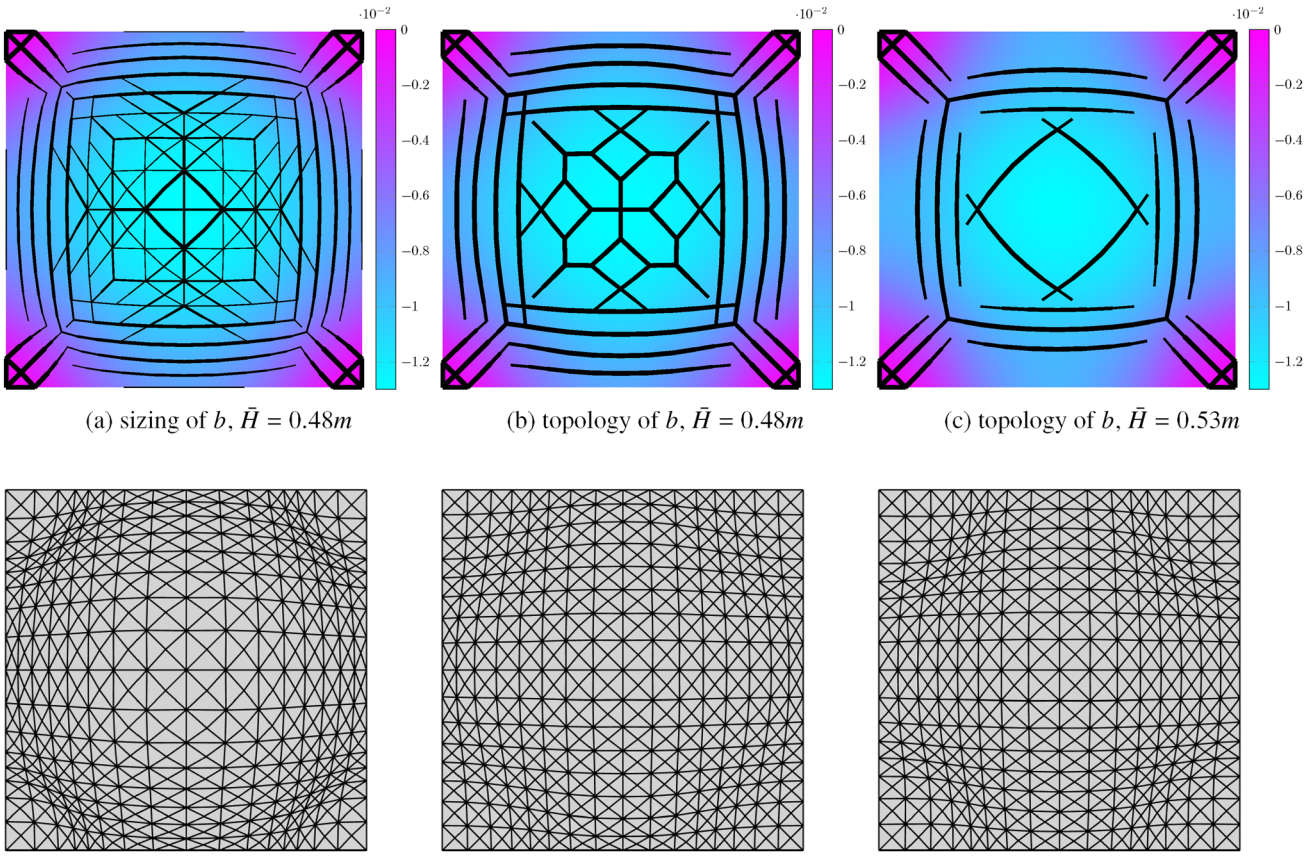

(a) sizing of b, $\bar{H} = 0.48m$ (b) topology of b, $\bar{H} = 0.48m$ (c) topology of b, $\bar{H} = 0.53m$

Fig. 10 Optimized layouts (black lines) and vertical displacements (colored map) of Example 2, a 10-by-10 plate fixed to four columns. The second row shows the optimized meshes

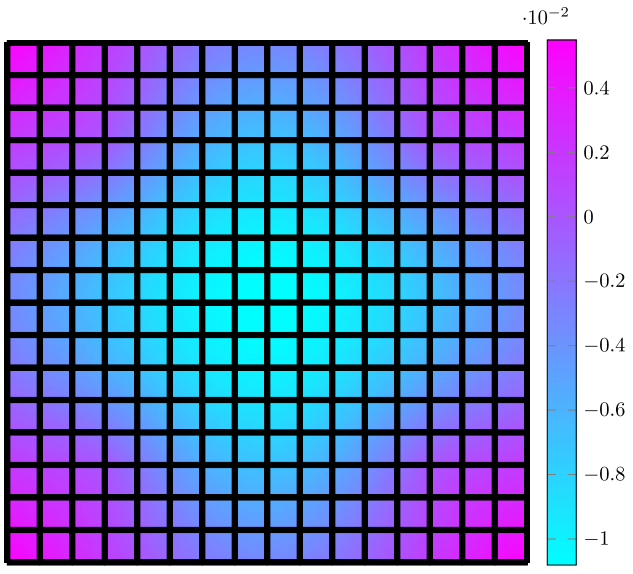

Fig. 11 Waffle-pattern reference design for a plate on four columns with cantilevers, Example 3. The volume is 12.48 m^3 and the maximum deflection is 0.0108 m

The boundary conditions for displacements and rotations, the restricted node movements for shape optimization and the initial mesh are sketched in Fig. 15. The initial mesh is the pattern of the reference design, consisting of 81 nodes, 208 edges and 128 triangles. In the initial design prior to optimization, the plate thickness is $t = 0.1$m, the beam height is $h = 0.2$m and all the beams are assigned $b_i = 0.1$m.

Table 6 and Fig. 16 show the results of three optimization runs. All runs are with a total depth of $\bar{H} = 0.4$m and a minimal plate thickness $\underline{t} = 0.07$m. Runs #1 and #2 are executed on a coarse triangulation with relatively large spacing between nodes, so they allow a higher maximum beam width and larger move limit for the nodes, as seen in Table 6. Run #3 uses a triangulation with double resolution to show the effect of mesh refinement, so $\bar{b}$ is decreased to 0.12 m and the move limit is the default value. The results show significant potential savings in material volume, exceeding 50% in all cases. These savings are primarily a result of allowing larger deflections along the edges as can be seen in Fig. 16. The feasible design space is utilized better and more regions are close to being active in the deflection constraint. In runs #1 and #2, it can be seen that the meshes hardly move. This is because of the relatively "stiff" boundary conditions for the

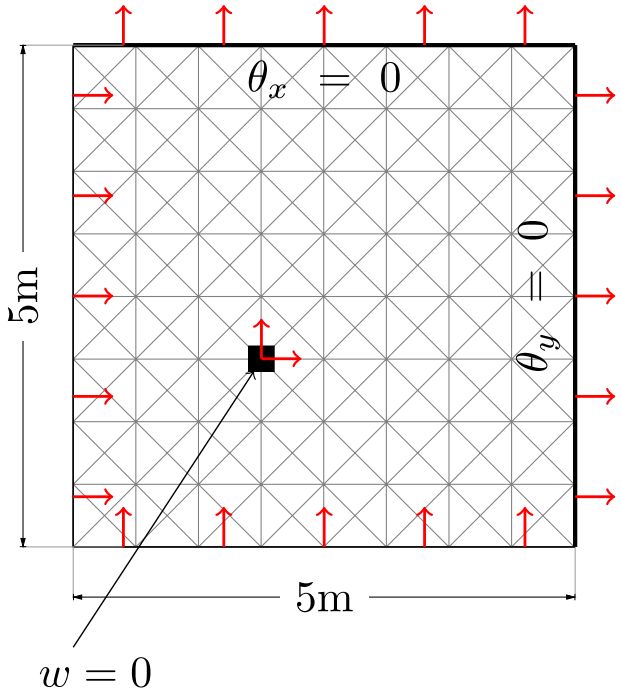

Fig. 12 Problem setup for the bottom left quarter of a plate on 4 columns with cantilevers, Example 3. The boundary conditions are stated along the symmetric edges and near the column. Red arrows represent restricted directions for node movements—the column's node and along the boundaries. Gray lines represent the initial mesh

mesh that restrict any movement along the edges, and perhaps also because the initial mesh accommodates nearly optimal beam directions. The refined mesh in run #3 enables an interesting pattern of curved ribs—resembling a post-processing of continuum topology optimization in the design of a box girder (Baandrup et al. 2020)—however, the quantitative benefit is small and the volume is only slightly lower than in run #1.

As observed in Fig. 16 (bottom right), mesh distortions may occur. This raises the question whether the optimizer exploits mesh distortions to achieve artificial plate stiffness and hence numerically improve the structural performance. To examine this effect, we manually remeshed the solution of run #3 such that triangles in the highly condensed and distorted region were replaced with healthier triangles, and a subsequent re-analysis was performed. The resulting displacement field and mesh pattern are presented in Fig. 17. The overall displacement field is the same, while the maximum displacement is $\delta = 0.0151$, only slightly higher than with the distorted mesh. This validates the quality of the optimized design, but at the same time also emphasizes the need for a more robust mesh optimization—as artificial stiffness is present.

6 Discussion

The purpose of this study was to present a computational procedure for optimizing ribbed plates, aiming at reducing their weight and indirectly also their embodied CO_2. The chosen design parameterization, that relies on a coupled plate-beam model and on the finite element mesh, allows to unify topology-, shape- and sizing optimization of ribbed plate systems—a unique feature in comparison to the literature. Another advantage of the parameterization is that it enables to optimize any plate domain as it uses a triangular mesh as a flexible ground structure for optimizing the layout of ribs. The main results are as follows:

1. Throughout several design examples, significant weight savings in the range of 24–57% have been demonstrated, compared to reasonable reference designs with regular ribbing patterns.
2. The weight reductions are achieved without increasing the total depth of the plate and imposing additional architectural compromise. In some cases, weight savings have been achieved together with reduction of the total depth.
3. The optimized designs show better utilization of the design space by bringing several regions close to the deflection constraint, while in the reference designs the maximal deflection is typically obtained in one region of the plate.

The results of this study, together with results from recent studies on ribbed plates (Whiteley et al. 2023; Huber et al. 2023; Ma et al. 2023), strengthen the argument in favor of ribbed plates as an environmentally-aware structural system. While the fabrication as reinforced or prestressed concrete plates may be costly, the tremendous reduction in quantity of raw materials motivates more detailed explorations. An interesting implication of the study is related

Table 5 Numerical results of Example 3

run	p_b	$\bar{H}$[m]	$\underline{t}$	iters	t[m]	h[m]	δ [m]	V [m^3]
#1	1	0.25	0.05	100	0.05	0.20	0.0108	8.5640 (-31%)
#2	3	0.25	0.05	100	0.05	0.20	0.0108	9.5142 (-24%)
#3	3	0.27	0.05	100	0.05	0.22	0.0108	8.7252 (-30%)

All runs use their minimal allowable t and maximal allowable depth H. The deflection constraint is satisfied precisely. The rightmost column includes the savings in volume, compared to the reference design

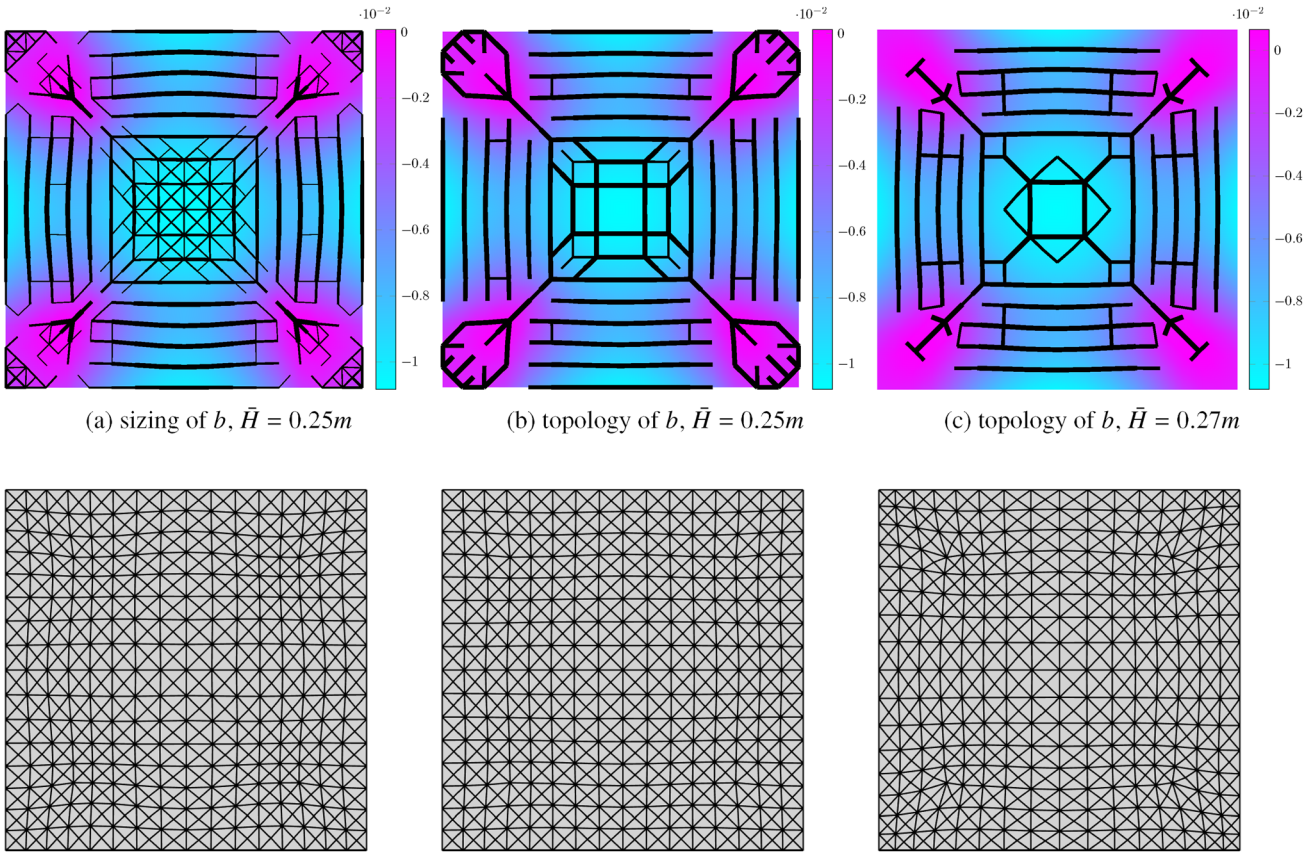

(a) sizing of b, $\bar{H} = 0.25m$ (b) topology of b, $\bar{H} = 0.25m$ (c) topology of b, $\bar{H} = 0.27m$

Fig. 13 Optimized layouts (black lines) and vertical displacements (colored map) of 10-by-10 plate, on four columns with cantilevers. The second row shows the optimized meshes

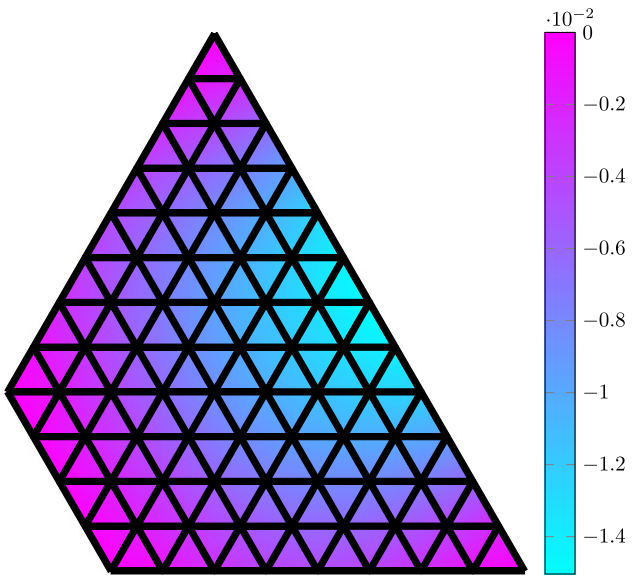

Fig. 14 Reference design (black lines) and vertical displacements (colored map) for a trapezoidal plate supported on four fixed columns at the vertices, Sect. 5.4. The volume is 12.62 m^3 and the maximum deflection is 0.0150 m

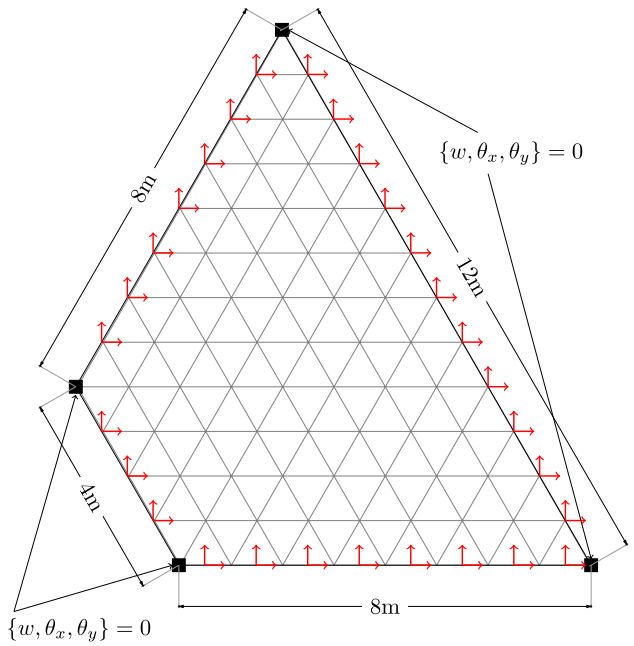

Fig. 15 Problem setup for the trapezoidal plate on 4 fixed columns, Example 4. The boundary conditions are stated for each of the columns. Red arrows represent restricted directions for node movements—along the perimeter. Gray lines represent the initial mesh

Table 6 Numerical results of Example 4

run	p_b	$\bar{b}$[m]	s_2[m]	iters	t[m]	h[m]	δ [m]	V [m^3]
#1	1	0.15	0.10	100	0.07	0.33	0.0150	5.4266 (-57%)
#2	3	0.15	0.10	100	0.07	0.33	0.0150	5.8831 (-53%)
#3	1	0.12	0.05	100	0.07	0.33	0.0150	5.3813 (-57%)

All runs use their minimal allowable t and maximal allowable depth H. The deflection constraint is satisfied precisely. The rightmost column includes the savings in volume, compared to the reference design

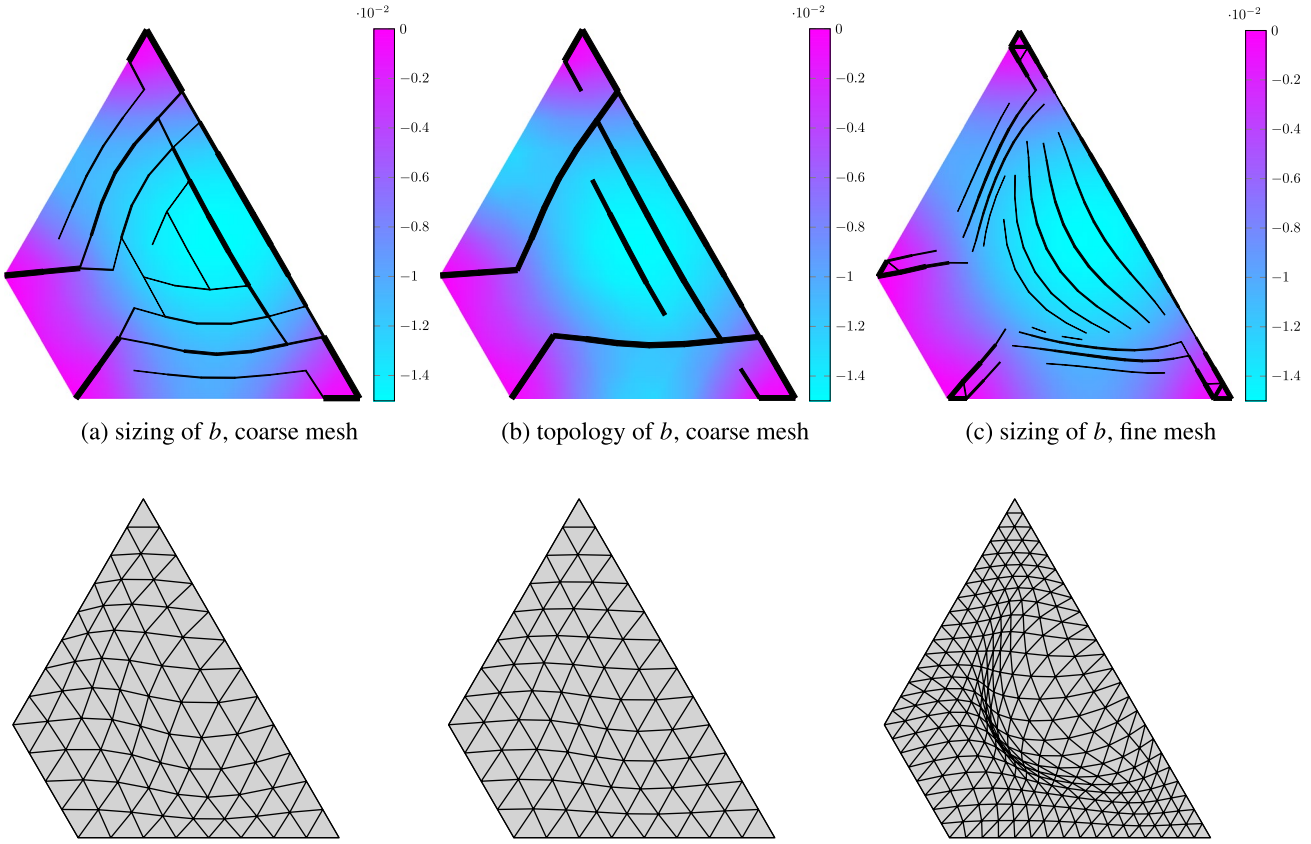

(a) sizing of b, coarse mesh (b) topology of b, coarse mesh (c) sizing of b, fine mesh

Fig. 16 Optimized layouts (black lines) and vertical displacements (colored map) of a trapezoidal plate, fixed to four columns at the vertices. The second row shows the optimized meshes

to the optimality of Nervi's patterns: using formal optimization, we do not obtain ribs in the directions of principal moments of a flat plate, and preliminary results with our mesh-based approach showed weight savings of roughly 10% beyond Nervi's savings, when compared to standard slabs (Majdouba 2022). Another important implication is the generality of the proposed procedure: while our focus herein is solely on concrete plates in buildings, the mesh-based approach is applicable in the much more general context of stiffened shells. Therefore, future work may expand the method towards thin and possibly curved shells that are stiffened by beams of arbitrary sizes, positioned in arbitrary locations and directions (e.g., Wang et al. 2017; Zhang et al. 2018; Savine et al. 2021).

As a first exploration of a new design parameterization and a corresponding optimization procedure, the study is bounded by several limitations. While our main application field is ribbed concrete plates, we limit ourselves to linear elastic modeling. This could suffice for preliminary design, but concrete cracking and reduced bending resistance should be taken into account to check the design for service limit state. Furthermore, detailed design of reinforcement for ultimate limit state as conducted by Whiteley et al. (2023) is out of the current scope. Nevertheless, weight savings

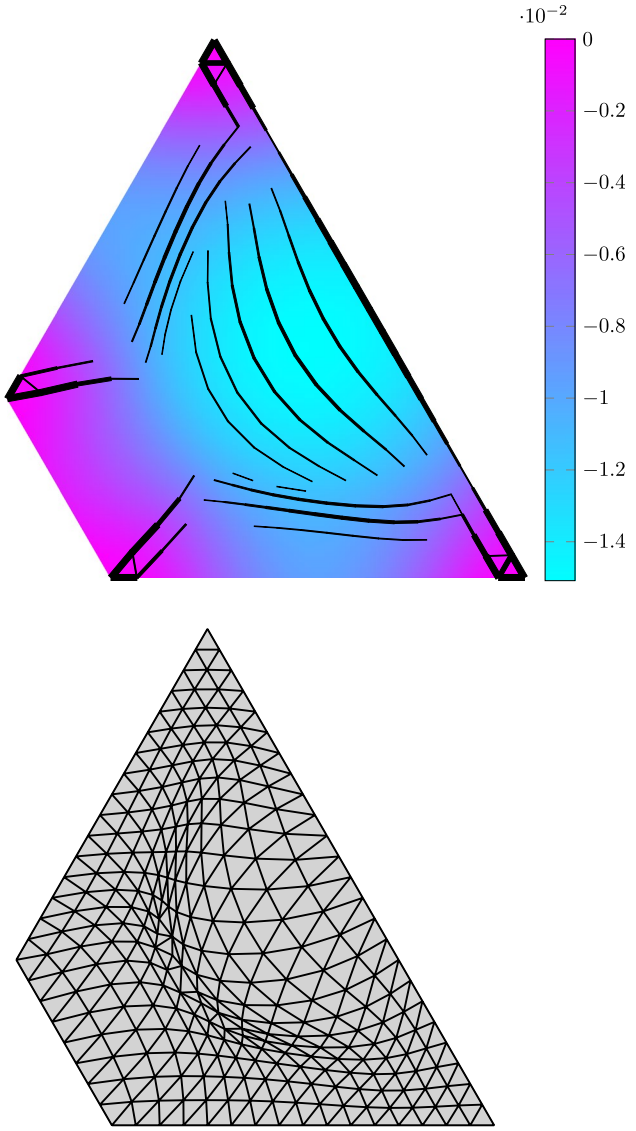

Fig. 17 Re-analysis of run #3 after mesh repairing. Top: the optimized layout (black lines) is superimposed upon the vertical displacements (colored map). Bottom: the repaired mesh. The displacement is less than 1% larger than with the distorted mesh

w.r.t reference designs are valid because they use the elastic deflection as a basis for comparison. We expect that the savings will not differ significantly when inelastic deformations will be modeled because the nonlinearity in service limit states is mild. Strength requirements could be integrated in an extension to the current formulation. The vanishing of beams and the number of constraints are expected to pose numerical challenges, that could be addressed by various techniques that have been developed in the context of topology optimization with stress constraints. Another limitation is the naive approach for controlling the mesh movement. This aspect of the optimization is rather delicate, and a more robust procedure for moving the mesh and avoiding excessive distortions should be adopted in future work.

Acknowledgements The authors are grateful to the anonymous reviewers for the thorough review and numerous helpful comments. The authors would like to thank Krister Svanberg for his implementation of MMA in MATLAB.

Funding Open access funding provided by Technion - Israel Institute of Technology.

Declarations

Conflict of interest The authors state that there are no Conflict of interest.

Replication of results All MATLAB codes used in this study are freely available through a public repository, https://zenodo.org/records/11489996.

References

Andrew RM (2019) Global CO_2 emissions from cement production, 1928–2018. Earth Syst Sci Data 11(4):1675–1710

Baandrup M, Sigmund O, Polk H, Aage N (2020) Closing the gap towards super-long suspension bridges using computational morphogenesis. Nat Commun 11(1):1–7

Bathe K-J (1996) Finite element procedures. Prentice Hall, Upper Saddle River

Batoz J-L (1982) An explicit formulation for an efficient triangular plate-bending element. Int J Numer Methods Eng 18(7):1077–1089

Batoz J-L, Bathe K-J, Ho L-W (1980) A study of three-node triangular plate bending elements. Int J Numer Methods Eng 15(12):1771–1812

Bolbotowski K, He L, Gilbert M (2018) Design of optimum grillages using layout optimization. Struct Multidisc Optim 58:851–868

Chang S-YP (1973) Analysis of eccentrically stiffened plates. University of Missouri-Columbia, Ph.D

Cook RD, Malkus DS, Plesha ME, Witt RJ (2001) Concepts and applications of finite element analysis, 4th edn. Wiley, New Jersey

Dorn W, Gomory R, Greenberg H (1964) Automatic design of optimal structures. J Mecanique 3:25–52

Eleftheriadis S, Duffour P, Greening P, James J, Stephenson B, Mumovic D (2018) Investigating relationships between cost and CO_2 emissions in reinforced concrete structures using

a BIM-based design optimisation approach. Energy Build 166:330–346
Field DA (1988) Laplacian smoothing and Delaunay triangulations. Commun Appl Numer Methods 4(6):709–712
Fuchs MB, Brull MA (1979) A new strain energy theorem and its use in the optimum design of continuous beams. Comput Struct 10(4):647–657
Gilbert M, Tyas A (2003) Layout optimization of large-scale pin-jointed frames. Eng Comput 20(8):1044–1064
Halpern AB, Billington DP, Adriaenssens S (2013) The ribbed floor slab systems of Pier Luigi Nervi. In: Proceedings of IASS annual symposia, vol. 2013, pp. 1–7. International Association for Shell and Spatial Structures (IASS), Madrid, Spain. Issue: 23
Huber T, Burger J, Mata-Falcón J, Kaufmann W (2023) Structural design and testing of material optimized ribbed RC slabs with 3D printed formwork. Struct Concr 24(2):1932–1955
Jayasinghe A, Orr J, Ibell T, Boshoff WP (2021) Minimising embodied carbon in reinforced concrete beams. Eng Struct 242:112590
Jeyachandrabose C, Kirkhope J, Babu CR (1985) An alternative explicit formulation for the DKT plate-bending element. Int J Numer Methods Eng 21(7):1289–1293
Ma J, He Y, Zhao Z-L, Xie YM (2023) Topology optimization of ribbed slabs and shells. Eng Struct 277:115454
Majdouba A (2022) Weight reduction of ribbed concrete slabs using structural optimization techniques. Master's thesis, Technion—Israel Institute of Technology, Haifa, Israel
Mathworks (2023) MATLAB Version 9.14.0.2239454 (R2023a). The Mathworks, Inc., Natick
Miller D, Doh J-H, Mulvey M (2015) Concrete slab comparison and embodied energy optimisation for alternate design and construction techniques. Constr Build Mater 80:329–338
Mróz Z, Rozvany G (1975) Optimal design of structures with variable support conditions. J Optim Theory Appl 15:85–101
Paya-Zaforteza I, Yepes V, Hospitaler A, Gonzalez-Vidosa F (2009) CO_2-optimization of reinforced concrete frames by simulated annealing. Eng Struct 31(7):1501–1508
Pressmair N, Xia Y, Wu H, Langelaar M, Hendriks MA, Majdouba A, Mogra M, Grisaro H, Amir O, Kromoser B (2023) Bridging the gap between mathematical optimization and structural engineering: design, experiments and numerical simulation of optimized concrete girders. Struct Concr. https://doi.org/10.1002/suco.202201096
Rozvany G (1972) Grillages of maximum strength and maximum stiffness. Int J Mech Sci 14(10):651–666
Rozvany GIN, Bendsoe MP, Kirsch U (1995) Layout optimization of structures. Appl Mech Rev 48(2):41–119. https://doi.org/10.1115/1.3005097
Savine F, Irisarri F-X, Julien C, Vincenti A, Guerin Y (2021) A component-based method for the optimization of stiffener layout on large cylindrical RIB-stiffened shell structures. Struct Multidisc Optim 64(4):1843–1861
Sigmund O, Zhou M, Rozvany G (1993) Layout optimization of large FE systems by new optimality criteria methods: applications to beam systems. In: Concurrent engineering: tools and technologies for mechanical system design, pp. 803–819. Springer, Berlin
Svanberg K (1987) The method of moving asymptotes-a new method for structural optimization. Int J Numer Methods Eng 24(2):359–373
Wang B, Tian K, Zhou C, Hao P, Zheng Y, Ma Y, Wang J (2017) Grid-pattern optimization framework of novel hierarchical stiffened shells allowing for imperfection sensitivity. Aerosp Sci Technol 62:114–121
Weaver W, Gere JM (2012) Matrix analysis of framed structures. Springer, New York
Whiteley J, Liew A, He L, Gilbert M (2023) Engineering design of optimized reinforced concrete floor grillages. Structures 51:1292–1304. https://doi.org/10.1016/j.istruc.2023.03.116
Yepes V, Gonzalez-Vidosa F, Alcala J, Villalba P (2012) CO_2-optimization design of reinforced concrete retaining walls based on a VNS-threshold acceptance strategy. J Comput Civil Eng 26(3):378–386
Zelickman Y, Amir O (2022) Optimization of plate supports using a feature mapping approach with techniques to avoid local minima. Struct Multidisc Optim 65:1–16
Zhang W, Liu Y, Du Z, Zhu Y, Guo X (2018) A moving morphable component based topology optimization approach for RIB-stiffened structures considering buckling constraints. J Mech Des 140(11):111404
Zienkiewicz OC, Taylor RL (2000) The finite element method: solid mechanics, vol 2. Butterworth-Heinemann, Oxford